SYNGAS PRODUCTION VIA STEAM REFORMING OF BIOETHANOL OVER Ni-BEA CATALYSTS: A BTL STRATEGY

Ilenia Rossetti[1*], Matteo Compagnoni[1], Elisabetta Finocchio[2], Gianguido Ramis[2], Alessandro Di Michele[3], Azzurra Zucchini[3], Stanislaw Dzwigaj[4,*]

[1]Dip. Chimica, Università degli Studi di Milano, INSTM Unit Milano-Università and CNR-ISTM, via C. Golgi, 19, I-20133 Milano, Italy

[2]Dip. di Ingegneria Civile, Chimica e Ambientale, Università degli Studi di Genova, P.le J.F. Kennedy 1, I-16129, Genova, Italy and INSTM Unit Genova

[3]Dip. di Fisica e Geologia- Università degli Studi di Perugia, Via Pascoli, 06123 Perugia

[4]Sorbonne Universités, UPMC Univ Paris 06, CNRS, UMR 7197, Laboratoire de Réactivité de Surface, F-75005, 4 place Jussieu, Paris, France

ABSTRACT

In this work we focused on syngas production from bioethanol, achieving proper $H_2/CO = 2$ ratio to feed the FT reaction. The catalysts were constituted by Ni supported over BEA zeolites. The Si/Al ratio was varied to assess the effect of acidity on catalyst activity, selectivity and stability. As well, the effect of Ni loading (0.6-4 wt%) was investigated.

Ni confinement into the zeolite pores proved a successful strategy to contrast deactivation by coking and to ensure stable operation with time-on-stream. Intermediate Ni loading (1.5

* Corresponding author: fax +39-02-50314300; e-mail: ilenia.rossetti@unimi.it.

- 4 wt%) allowed to limit byproducts formation and to achieve the desired H_2/CO ratio (ca. 2 mol/mol) for the present application. By contrast, increasing Ni loading increased the activity for both the reforming and the water gas shift reactions, thus improving H_2 productivity but unbalancing the reaction mixture for application in the FT process. The conversion of CO through the WGS reaction showed strongly correlated to Ni loading, as well as the reforming of methane, a byproduct of bioethanol decomposition. The equilibrium conversion was achieved at the highest Ni loading.

Keywords: Bioethanol steam reforming; H_2 production; Ni catalysts; BEA zeolite; Syn gas production; Fischer Tropsch.

1 – INTRODUCTION

Bioethanol production is constantly growing and in recent years it is moving towards a second generation production concept [1,2]. Besides using it as fuel or fuel additive, great research efforts have been focused on bioethanol steam reforming (SRE) in view of a sustainable H_2 production [3–7]. However, in order to effectively promote the biorefinery concept, it is compulsory to find out suitable and sustainable strategies also for the production of chemicals from renewable materials. Ethanol is an interesting candidate since it may be rather easily converted to syngas through steam reforming. It is also easier to transport and handle with respect to different biomass derived feedstocks. The CO/H_2 mixture (syngas) can be then converted to various hydrocarbons by means of the well assessed Fischer Tropsch process (FT). Usually, the steam reforming process applied to ethanol is pushed toward the highest H_2 productivity. Indeed, up to now the main objective of the research in this field was H_2 production with the final scope of feeding fuel cells systems through renewable feedstocks. Thus, catalysts and operating conditions were

searched to favor the water gas shift reaction (WGS), which converts CO to CO_2 with further H_2 production [8–10].

On the contrary, the FT process may be efficiently carried out starting from a CO richer mixture (H_2/CO = 2) and, ideally, the selectivity to longer hydrocarbon chains may be improved at even lower H_2/CO ratio [11]. This implies that ethanol steam reforming catalysts should be optimised for this specific application, *e.g*. unfavouring further CO conversion through the WGS reaction.

In the present work, we concentrated on the selection of catalysts that may produce syngas through the steam reforming reaction, specifically leading to a low H_2/CO ratio suitable for the FT process. The optimisation of catalyst formulation and process conditions aims at developing an integrated process for the production of important bulk chemicals from this renewable feedstock.

Different active phases have been proposed for the steam reforming of ethanol and Ni and Co were evidenced as the most promising among non noble metals [12–21]. Catalyst stability issues have been also taken into account, since sintering, coke deposition over acidic sites and the formation of carbon filaments may deeply affect catalyst performance [3,7,19,22–25]. In particular, coke formation may occur through many different pathways, recently reviewed by Mattos et al. [7] and occurring under different operating conditions. For instance, ethanol dehydration may take place over acidic sites, which may also catalyze ethylene polymerization to form coke. On the other hand, Ni and Co are very well known to form carbon filaments if carbide intermediates accumulate subsurface. Typically, filaments formation is faster over big metal particle size [23,24,26–35]. Therefore, suitable strategies to limit coke accumulation are acidity control (*e.g.* by adding a basic promoter [13,33]) and the improvement of metal dispersion. The latter may be tuned on the basis of metal-support interaction: the strongest the latter, the highest the metal dispersion. Furthermore, a strong

interaction helps stabilising the metal particles towards sintering under the high temperature operating conditions for SRE [23,24,33,34].

In the present work, we selected an alternative approach to solve these problems. In order to improve metal dispersion we tried to disperse it in a high surface area matrix such as a zeolite. The microporous channels have been selected to entrap Ni preventing its extensive sintering during operation. Variable Ni loading allowed to further tuning metal dispersion. Furthermore, the acidity issue was taken into account by preparing different zeolites with two different initial Si/Al ratio and by further dealuminating them. We selected a zeolite since in previous investigations we obtained interesting results when using a mesoporous SBA15 silica as support [24,35]. However, in such case the mesoporous structure did not allow a proper confinement of the active phase. Therefore, we turned our attention to a BEA microporous structure constituted by channels *ca.* 6.7 Å in size. They are intrinsically larger than MFI, better allowing the diffusion of ethanol [36]. Almost all the accessible free volume of the pores is available given the characteristic molecular size of ethanol (*ca.* 3.8 Å) [37].

Ethanol steam reforming has been carried out with Ni/ITQ-2 dealuminated zeolite [38], modified mordenite [39], zeolite Y [40–42] and faujasite [43]. However, to our knowledge BEA zeolites were never used for this application. The prepared catalysts have been characterized by various techniques and then tested for the production of syngas under variable reaction conditions.

2 – EXPERIMENTAL

2.1 – Catalyst preparation

Nine different samples of Ni/BEA have been prepared starting from commercial zeolite supports, characterized by different acidity (Al content) and Ni loading.

Tetraethylammonium BEA (TEABEA) zeolites with Si/Al ratio of 12.5 and 17 (mol/mol) provided by RIPP (China) were calcined in air (100 °C/h) at 550°C for 15 h under static conditions to remove the organic template. Both the organic-free BEA zeolites were then treated two times with 400 mL of 0.1 mol/L NH_4NO_3 solution during 3 h in order to exchange K^+ and Na^+ ions present in industrial BEA zeolite with NH_4^+ ion. Then, the solids were washed with distilled water and dried overnight at 90°C. The NH_4AlBEA samples were calcined in air (100 °C/h) for 3 h at 500°C under static conditions to remove NH_3 and obtain the acidic form of the zeolite BEA, HAlBEA (I) and HAlBEA(II), with Si/Al ratio of 12.5 and 17 (mol/mol), respectively.

The treatment of the TEABEA zeolites with Si/Al ratio of 12.5 and 17 (mol/mol) with nitric acid (13 mol/L) at 80°C under stirring in air lead to removing of the organic template (TEA) and Al atoms. The treatment has been carried out for short (0.08 h, partial dealumination) or prolonged time (4 h, deep dealumination).

Ni was added by wet impregnation from a $Ni(NO_3)_2 \cdot 6H_2O$ solution. Proper amount of Ni precursor was dissolved in 200 mL water and the solid suspension was stirred for 24 h at r.t. at pH of 3.3. Then, the suspension was stirred in evaporator under vacuum of a water pump for 2 h in air at 60°C until the water was completely evaporated.

2.2 - Characterisation

X-ray powder diffraction (XRD) analysis was carried out at room temperature by means of a PHILIPS PW1830 diffractometer with Bragg-Brentano θ - 2θ geometry Fig. 1. The Cu$K\alpha$ radiation (λ = 1.5406 Å) was used. Intensities were collected over a 21° – 90° 2θ range with 0.03° step size and 4 s step time. The apparatus was provided with graphite monochromator. The voltage and current intensity of the generator were set at 40 kV and

30 mA respectively. The Rietveld method [44] was used for the XRPD data refinement using TOPAS software [45].

Specific surface area and pores size distribution were evaluated trough N_2 adsorption-desorption isotherms at -196°C (Micromeritics, ASAP 2020). Surface area was calculated on the basis of the BET equation, whereas the pores size distribution was determined by the BJH method, applied to the N_2 desorption branch of the isotherm. Micropores volume and area were determined from the t-plot analysis. Prior to the analysis the sample was outgassed at 300°C overnight.

The Temperature Programmed Reduction (TPR) technique was employed to identify different metallic species possibly present in the catalysts according to the different reduction temperatures, in case used to assess the interaction strength between the active phase and the support. The catalyst was placed in a quartz reactor and heated by 10°C/min from *r.t.* to 800°C in a 5% H_2/Ar mixed gas stream flowing at 40 mL/min. Temperature Programmed Oxidation (TPO) was carried out on the reduced sample by feeding 40 mL/min of 10 vol% O_2/He gas mixture while heating by 10°C/min from r.t. to 800°C.

SEM images have been obtained using a Field Emission Gun Electron Scanning Microscopy LEO 1525, after metallization with Cr. Elemental composition was determined using a BrukerQuantax EDS.

TEM images have been obtained using a Philips 208 Transmission Electron Microscope. The samples were prepared by putting one drop of an ethanol dispersion of the catalysts on a copper grid pre-coated with a Formvar film and dried in air.

FT-IR spectra have been recorded in static conditions by a Nicolet Nexus Fourier transform instrument, using conventional IR cells connected to a gas manipulation apparatus. Pressed disks of pure catalyst and support powders (~30 mg) were activated by prolonged

outgassing at 500°C. Pyridine (py, Aldrich, pur. 98%) adsorption experiments have been performed over the activated samples at room temperature and following outgassing at increasing temperatures.

2.3 Activity testing for Ethanol Steam Reforming (ESR)

Details on the equipment for activity testing have been previously reported elsewhere [23]. The catalysts (*ca*. 0.5 g, 0.15-0.25 mm particle size) were diluted 1:3 (vol/vol) with SiC of the same size. The void space of the reactor was filled with quartz beads, *ca.* 1mm in size. The catalyst was activated in 50 cm^3/min (STP) of a 20% H_2/N_2 gas mixture, while heating by 10°C/min up to 800°C for 1 h.

Activity testing was carried out by feeding 0.017 cm^3/min of a 3:1 (mol/mol) $H_2O:CH_3CH_2OH$ liquid mixture by means of a Hitachi, mod. L7100, HPLC pump, added with 56 cm^3/min of N_2, used as internal standard, and 174 cm^3/min (STP) of He. Such dilution of the feed stream was calibrated so to keep the reactants mixture in the vapour phase even at zero conversion at the reactor outlet.

The activity tests were carried out at atmospheric pressure, GHSV = 2500 h^{-1} (referred to the ethanol + water gaseous mixture, corresponding to 63400 h^{-1} if referred to the total gas flow rate) at 750°C and at 625°C for some interesting samples.

The analysis of the out-flowing gas was carried out by GC analysis. Repeated analyses of the effluent gas were carried out every hour and the whole duration of every test at each temperature was *ca*. 8 h. The raw data, expressed as mol/min of each species outflowing from the reactor, averaged after 4-8 h-on-stream, have been elaborated as better detailed elsewhere [23].

3 - RESULTS AND DISCUSSION

3.1 – Textural, structural and morphologic properties

The list of samples prepared is reported in Table 1. The codes represent the Ni loading and the dealumination degree (HAl meaning acidic, SiAl partially dealuminated and Si deeply dealuminated samples). Numerical codes are also added for rapid labelling in Figures and Tables.

N_2 adsorption-desorption evidenced the typical isotherms of microporous materials with an evident hysteresis. BET surface area was between 320 and 360 m^2/g for every catalyst, with a main contribution of micropores (Table 1). Pore size distribution was entirely centred below 5 nm. The amount of Ni loaded did not significantly affect surface area.

XRD patterns are reported in Fig. 1 for all the prepared samples. The Rietveld method [44] was used for the XRPD data refinement using TOPAS software [45], which models the X-ray powder diffraction profile shape by a convolution between diffractometer profile functions, that is, geometric instrument profile and wavelength profile functions, and sample broadening functions (Fundamental Parameter Approach) ([46] and references therein). The refined parameters were: the background (fitted with 13-term Chebyshev polynomial function), sample absorption, average crystallite size (assuming Lorentzian contribution to broadening), scale factor and unit cell parameters.

The recognized mineral phases within the analysed samples are the A, B and C polymorphs of BEA zeolites. Data refinements were carried out starting from atomic coordinates and cell parameters from Newsam et al. [47] for A and B polymorphs of BEA zeolites and Corma et al. for C polymorph of BEA zeolites [48]. Results are listed in Table 2 together with the R_p, R_{wp} and R_{bragg} accordance parameters [49]. The polymorph A was the predominant (*ca.*

50%), followed by B (25-30%) and C (20-25%). The proportion between the different crystal structures was not correlated to the thermal/chemical treatment and Ni concentration.

Temperature programmed reduction-oxidation-reduction (TPR-TPO-TPR) cycles have been performed on every sample. An example of the results for $Ni_{1.5}$SiBEA(II) (sample 9) is reported in Fig. 2. The fresh sample reduced in one step (TPR1, Fig. 2) below 450°C. The peak profile was relatively sharp, indicating substantial homogeneity of the Ni species. The second TPR collected after oxidation of the reduced sample evidenced a rather different behavior. Two reduction features are presented, a broad one centred around 560°C and a second sharper one centred at *ca*. 607°C. This means that some redispersion occurred for Ni, which developed a strong interaction with the support after activation at high temperature. Reasonably, the reoxidation at high temperature may induce the formation of Ni-silicate, thus favoring the redispersion of Ni and the strengthening of its interaction with the support. However, due to the very low Ni content this was not evidenced when characterizing by XRD the samples activated at 500°C and 800°C. The same XRD patterns have indeed evidenced that the crystal structure was kept almost unaltered upon activation and TEM confirmed that no significant sintering occurred. Furthermore, the broadening of the peaks and the presence of multiple reduction features is an index of heterogeneity of the active sites. The ones more dispersed and more strongly interacting with the support are expected to reduce at higher temperature and vice-versa [23,24,30–35].

The results for all the samples are summarised in Table 3 reporting the temperature range of each peak and the relative maximum.

In general, an increase of Ni content induced a decrease of the reduction temperature both in TPR1 and TPR2 (compare samples 6,7,5 and 3,9,4). This is in line with the expected decrease of dispersion with increasing concentration of Ni. By contrast, when increasing the Al content, *i.e.* acidity of the sample, the reduction pattern was generally shifted to lower temperature, indicating a lower dispersion. This means that Al content induced a weakening

of the metal-support interaction. Furthermore, the redispersion phenomenon upon activation which was described *e.g*. for $Ni_{1.5}$SiBEA(II) catalyst (sample 9) (shift to higher temperature of the TPR2 pattern with respect to TPR1) was favored at high Si/Al ratio (deep dealumination), being much less evident for samples 1 and 8.

Low nickel reducibility, *i.e.* high dispersion and strong interaction of nickel with the support, is often beneficial for activity and most of all for stability towards coking. Indeed, the latter may be ascribed in part to the formation of carbon filaments over Ni particles and it is much more favored when Ni particle size is bigger.

Thus, on the basis of the collected results, a low Ni content and a high Si/Al ratio should be preferred to improve dispersion and to strengthen the metal interaction with the support.

TEM images were collected for every sample and confirmed the conclusions of TPR analysis. The catalyst particles were generally constituted by agglomerates of nanoparticles 20-100 nm in size, as shown in Fig. 3. This particle size would allow to reduce mass transfer limitations inside the zeolite pores and to make most of the active sites available for the reaction. The identification of Ni/NiO particles was very hard even after reduction, due to the low Ni content and very high dispersion. Fig. 3*a* represents the dependence of particle size on Ni loading for both series of catalysts. Very small Ni particles (< 5 nm) were hardly observed only for samples 4 and 5, characterized by the highest metal content (evidenced by arrows). However, we also noticed a strong correlation of dispersion on the Si/Al ratio (Fig. 3*b*). Indeed, metal particles were not evident at all for samples 2 and 9 (Ni = 1.5 wt%, prepared from the two deeply dealuminated BEA), whereas they were visible at the same metal loading for the two samples characterized by lower Si/Al ratio. This fairly confirms the TPR conclusion that the highest dispersion may be reached by increasing the Si/Al content, likely favoring the formation of a stable Ni-silicate.

The redispersion upon activation was also checked by TEM. We report in Fig. 3*c* the effect of reduction under H_2 flow at 800°C for sample 1, which evidences that the Ni particles found in Fig. 3*b*, completely disappeared after activation.

3.2 – Catalysts characterization by FT IR

FT IR spectra of BEA surface and probe molecules adsorption have been performed in order to understand the modifications induced by thermal treatments and their effect on the catalytic activity. The spectra of pure samples 1, 2, 3 and 8, 9 recorded after outgassing at 500°C are reported in common scale in Fig. 4, focusing on the OH stretching region. The spectra of samples 1 and 8 (calcined samples) are characterized by a quite complex pattern of bands, consisting of a main adsorption at 3740 cm^{-1}, possibly complex, and by two weak components at 3670 and 3605 cm^{-1}, completely consistent with the spectra reported for H-BEA materials after calcination [50–53]. The main band has been assigned to the stretching mode of terminal Si-OH groups thought to be located mainly at the external crystal surface. Its complexity should arise from the formation of two different families of silanol groups. The band at 3605 cm^{-1} is assigned to bridging Al-OH-Si groups commonly associated to the Brønsted acidity of these materials, in particular to OHs in the internal sinusoidal channels of H-BEA [50], whereas the component at 3670 cm^{-1} is assigned to Al-OH groups of Al ions in extraframework position. The detection of a very weak band at 3780 cm^{-1} suggests that also another kind of Al-OH extraframework species are formed, having different coordination states.

The spectrum of sample 8 shows a shaper component at 3739 cm^{-1}, without the enlargement detected for the sample 1 peaks. This evidences the formation of a single type of silanol groups over the catalyst surface. Moreover, we can notice that sample 8 spectrum is lacking of the high frequency band, assigned to extraframework Al. Therefore, in spite of the similar

Si/Al ratio (Table 1), a starting material with lower Al allows its better allocation into the framework. As detailed in the next paragraph, extraframework alumina species were not directly connected to catalytic performance, except for the general influence of sample acidity on coking.

In this spectral region, for samples 2,3 and 9 (after dealumination treatment) we found only one main band centred at 3730 cm^{-1}, clearly formed by two components and tailing to lower frequencies, while the components below 3700 cm^{-1} disappeared. In particular, the disappearance of the band at 3605 cm^{-1} due to bridging OHs corresponds to the observed disappearance of the Brønsted acidity. This effect points out the dealumination strongly affecting the framework structure [51,52]. Moreover, deep dealumination (samples 3 and 9) leads to a reduction of the overall OH bands intensity.

FT IR spectra of absorbed pyridine confirm that the extended dealumination of samples 2, 3 and 9 changes of the amount and the nature of surface acidic sites. In fact on these samples Brønsted acidity as well as the strongest Lewis sites are not present.

3.3 – Activity testing for Ethanol Steam Reforming

The catalytic activity of these samples was tested for the steam reforming of ethanol at 750°C. We particularly focused on syngas production with $H_2/CO = 2$, suitable for chemicals production through the FT process. The 3:1 (mol/mol) water/ethanol ratio corresponds to *ca*. 50 vol% solutions, which are easily obtainable from the bioethanol fermentation broth through a flash drum. This allows using a much less expensive feedstock than heavily dehydrated ethanol, considering that bioethanol purification account for 50-80% on its production costs [8].

The results have been collected in Tables 4 and 5.

The equilibrium composition has been also calculated by using the ASPEN Plus (V.8.8) simulation software. The simulation has been carried out by using a Gibbs reactor block. This approach consist in the definition of the components which may be present (either as reactants, inert or products) in the reactor to define the equilibrium composition without assumptions on the specific reactions taking place. The Gibbs reactor was operated at 750°C, 1 atm, fed with the actual reacting mixture (including intert gas). The calculated values are reported in the same values.

3.3.1 - Effect of acidity

We compared samples with the same Ni content (1.5 wt%), but different Si/Al ratio, so characterized by different acidity, *i.e*. samples $Ni_{1.5}$HAlBEA(I), $Ni_{1.5}$HAlSiBEA(II), $Ni_{1.5}$HAlBEA(II) and $Ni_{1.5}$SiBEA(II) (catalysts 1, 2, 8 and 9).

Based on the Si/Al ratio (Table 1) and on the depth of dealumination treatment, we expected the following acidity scale, perfectly confirmed by FT-IR analysis: 1 ($Ni_{1.5}$HAlBEA(I), strong Brønsted acidity, mainly), > 8 ($Ni_{1.5}$HAlBEA(II), strong Brønsted acidity, mainly) > 2 ($Ni_{1.5}$HAlSiBEA(II), traces of Brønsted acidity), > 9 ($Ni_{1.5}$SiBEA(II) acidity substantially suppressed). This is in line with the Al content, decreasing in this order (Table 1).

At 750°C full ethanol conversion was achieved for every sample under the specified reaction conditions. Some CH_4 was always present, formed by ethanol decomposition but incompletely reformed. H_2 productivity was not the highest achievable due to the fact that this set of sample was poorly active for the water gas shift (WGS) reaction and did not reach full methane conversion. Indeed, CO_2 was almost absent in the product distribution and the selectivity to CO and H_2 was almost equal. This result may be ascribed to the low Ni loading of these samples (*vide infra*). As desired, this leads to optimal H_2/CO ratio for the production of chemicals through the FT reaction.

The highest H_2 productivity has been observed for sample 2 $Ni_{1.5}$HAlSiBEA(II) due to its better activity for the WGS reaction (as testified by the negligible CO/CO_2 ratio) and for the reforming of methane (lowest selectivity of the series). This may be an interesting result if the main goal is the production of H_2, but it induces a misbalance between CO and H_2 selectivities if the purpose is the FT valorisation of the syngas produced from ethanol, as in the present case. In any case, the CO/CO_2 ratio may be also tuned by modifying temperature. For instance, sample 1 $Ni_{1.5}$HAlBEA(I) tested at 625°C led to $CO/CO_2 = 6.7 \pm 0.6$ (mol/mol).

As expected, the C balance was around 100% for every sample tested at 750 and 625°C, irrespectively of acidity. Indeed, at such high temperature the carbon deposits possibly accumulated over the catalyst surface may be easily gasified. In general, the performance of this set of catalysts was rather similar, suggesting that acidity does not play a key role when operating steam reforming at high temperature.

An additional test was performed by lowering the contact time (GHSV = 3655 h^{-1}) on sample 1 $Ni_{1.5}$HAlBEA(I), *i.e.* the most acidic, thus in principle more critical as for deactivation by coking. The effect of sample acidity manifested in the massive formation of ethylene, which was not effectively reformed at decreased contact time. Thus, increased acidity favors the ethanol dehydration pathway to form ethylene.

At last, it should be underlined that stability problems may arise when dealing with high Al-loaded zeolites at high temperature in wet atmosphere. Since the main hydrothermal stability problem is typically related to dealumination by effect of steam, this is not considered really relevant here, at least for the deeply dealuminated samples.

3.3.2 - Effect of Ni loading

A first set of samples was prepared starting from a native Si/Al = 17, followed by deep dealumination (samples 3 $Ni_{0.6}$SiBEA(II), 9 $Ni_{1.5}$SiBEA(II) and 4 $Ni_{3.0}$SiBEA(II)), whereas a

second series was prepared from the BEA structure originally containing Si/Al = 12.5, followed also in this case by deep dealumination (samples 6 $Ni_{0.7}$SiBEA(I), 7 $Ni_{1.0}$SiBEA(I) and 5 $Ni_{4.0}$SiBEA(I)). In this case, we may consider the effect of acidity as limited. Results are reported in Table 5.

For the first group of samples tested at 750°C, the C balance was similar and ethanol conversion was 100% in every case. As mentioned earlier, this is expected in virtue of the high operating temperature.

In contrast to acidity, Ni loading deeply affected catalyst performance. H_2 productivity increased with Ni content and correspondingly the CO/CO_2 ratio decreased. These two parameters are of course correlated, since they both suggest increasing activity for the steam reforming and WGS reactions with increasing metal loading. The equilibrium values have been reached at the highest Ni loading, explaining the reasons of plateau values in Fig. 5 and 6.

More precisely, at the lowest Ni loading unreformed ethylene was present even at such a high temperature, but it was completely reformed for the samples with the highest Ni loadings. Accordingly, some unreformed methane was still present for every sample, but its selectivity systematically decreased with increasing concentration of the active phase.

By looking at Fig. 5 one may observe that both the selectivity to CH_4 and the CO/CO_2 ratio decreased with increasing Ni content, index of increasing reactivity for the methane steam reforming and WGS reactions, respectively. The trends clearly reached a plateau value at 3-4 wt% Ni, sufficient to ensure satisfactory activity for this application. This plateau was indicative of nearly equilibrium composition of the outlet gas (Table 5).

A similar conclusion may be inferred by considering water conversion and H_2 productivity, both increasing with Ni loading (Fig. 6). It should be remarked that increasing activity for H_2 production is possible by further increasing Ni loading to 10 wt%. Indeed, this sample led to

CO/CO_2 = 2.9 (mol/mol) and completely converted methane, so enhancing hydrogen productivity, but leading to an unbalanced reaction mixture for the FT reaction.

No significant stability issues were evident at this operating temperature and the C balance was satisfactory for each catalyst. This in an important feature, which can be correlated in part with the high operating temperature, which favours the gasification of possible C accumulated, in part to the very high dispersion of Ni achieved with the present samples. Ni stabilisation by the support is an additional feature, revealed by TPR and TEM, which induces stable and productive operation at high SRE temperature.

The same results have been achieved when testing samples 6 $Ni_{0.7}$SiBEA(I), 7 $Ni_{1.0}$SiBEA(I), 5 $Ni_{4.0}$SiBEA(I) prepared with variable Ni loading, but with an initial Si/Al ratio = 12.5, followed by dealumination (Table 5, Fig. 5 and 6).

As a final remark we can conclude that active catalysts for syngas production have been prepared by dispersing low loading Ni over BEA zeolites. Too low Ni concentration led to unacceptably high outflow of byproducts, such as ethylene and methane (Fig.7a). Their concentration may be limited by increasing Ni loading, as shown in Fig. 7b, leading also to increasing H_2 productivity. However, if the goal is to optimize H_2/CO molar flows to feed the FT process and produce a wide range of chemicals starting from bioethanol as renewable raw material, relatively low Ni loading has to be selected. Increasing Ni loading promotes the WGS reaction and increases H_2/CO, as reported in Fig. 8 for both support series. Therefore, for the present scope, Ni loading 1.5 wt% leads to sufficient reforming activity to convert all ethanol, ethylene and to achieve sufficiently low selectivity to CH_4 (5-6%). The desired H_2/CO ratio to feed the FT process can be successfully reached at this metal loading.

4 – CONCLUSIONS

Incorporation of Ni in BEA zeolite, with different acidity and low metal loading allowed the pathway *bioethanol-to-hydrocarbons via FT reaction*.

A set of Ni-based catalysts supported over BEA zeolite was prepared and used for the steam reforming of ethanol. Ni loading and the Si/Al ratio were varied and affected catalyst performance. High temperature activity testing (625-750°C) evidenced full ethanol conversion, but the permanence of unreformed by-products at low Ni loading. Increasing Ni amount positively affected both the catalytic activity for methane steam reforming and for the water gas shift reactions, leading to increasing H_2 productivity. Catalyst acidity, determined essentially by the Si/Al ratio, was not a determinant parameter during high temperature operation. Poor residual acidity remained after dealumination treatments, which induced the removal of both extraframework acidic Al ions and Al framework sites, therefore inducing the disappearance of strong Brønsted acidic sites (bridiging Si-(OH)-Al species).

The poor residual acidity was in case sufficient to promote ethanol dehydration to ethylene, but it was not sufficient to promote its accumulation in form of coke, as testified by full C balance and unreformed ethylene outflowing the reactor (*i.e*. at low Ni loading or shorter contact time).

In order to promote the ethanol to hydrocarbons route in an integrated biorefinery concept, the activity to WGS should be limited as much as possible, together with elimination of byproducts which may limit the overall process efficiency. Therefore, operation at high temperature (e.g. > 600 °C) with intermediate Ni loading (ca. 1.5 wt %) promotes the production of syngas with proper H_2/CO ratio to feed the FT process. It should be also underlined that the water/ethanol feeding ratio here adopted allows to use a *ca.* 50 vol% bioethanol solution obtained by preliminary flash separation of the fermentation broth, promoting the use of a less purified and less expensive raw material.

The catalytic systems proposed here succeeded in attaining high metal dispersion thanks to the high surface area of the starting material and the confinement of Ni into the zeolite

structure. This provides good metal dispersion and stability with respect to sintering. In addition, these results lead to the interesting conclusion that metal redispersion may be achieved upon activation, so further improving going towards an improvement of the resistance to coking.

REFERENCES

[1] G. Koçar, N. Civaş, Renew. Sustain. Energy Rev. 28 (2013) 900–916.

[2] http://www.gruppomg.com/en/news/10, (n.d.).

[3] M. Ni, D.Y.C. Leung, M.K.H. Leung, Int. J. Hydrogen Energy 32 (2007) 3238–3247.

[4] J.-J. Hwang, Renew. Sustain. Energy Rev. 19 (2013) 220–229.

[5] N. Bion, D. Duprez, F. Epron, ChemSusChem 5 (2012) 76–84.

[6] P. Panagiotopoulou, D.I. Kondarides, X.E. Verykios, Ind. Eng. Chem. Res. 50 (2011) 523–530.

[7] L. V. Mattos, G. Jacobs, B.H. Davis, F.B. Noronha, Chem. Rev. 112 (2012) 4094–4123.

[8] I. Rossetti, J. Lasso, M. Compagnoni, G. De Guido, Chem. Eng. Trans. 43 (2015) 229–234.

[9] I. Rossetti, M. Compagnoni, M. Torli, Chem. Eng. J. 281 (2015) 1036–1044.

[10] I. Rossetti, C. Biffi, G.F. Tantardini, M. Raimondi, E. Vitto, D. Alberti, Int. J. Hydrogen Energy 37 (2012) 8499–8504.

[11] Y. Lu, T. Lee, J. Nat. Gas Chem. 16 (2007) 329–341.

[12] A.C. Basagiannis, X.E. Verykios, Appl. Catal. A Gen. 308 (2006) 182–193.

[13] A.N. Fatsikostas, X.E. Verykios, J. Catal. 225 (2004) 439–452.

[14] A.N. Fatsikostas, D.. Kondarides, X.E. Verykios, Catal. Today 75 (2002) 145–155.

[15] D.K. Liguras, D.I. Kondarides, X.E. Verykios, Appl. Catal. B Environ. 43 (2003) 345–354.

[16] L.J.I. Coleman, W. Epling, R.R. Hudgins, E. Croiset, Appl. Catal. A Gen. 363 (2009) 52–63.

[17] M. Benito, R. Padilla, a. Serrano-Lotina, L. Rodríguez, J.J. Brey, L. Daza, J. Power Sources 192 (2009) 158–164.

[18] V. a. Kirillov, V.D. Meshcheryakov, V. a. Sobyanin, V.D. Belyaev, Y.I. Amosov, N. a. Kuzin, a. S. Bobrin, Theor. Found. Chem. Eng. 42 (2008) 1–11.

[19] X. Zhao, G. Lu, Int. J. Hydrogen Energy (2016).

[20] S.C. Dantas, K.A. Resende, C.N. Ávila-Neto, F.B. Noronha, J.M.C. Bueno, C.E. Hori, Int. J. Hydrogen Energy 41 (2016) 3399–3413.

[21] G.Y. Ramírez-Hernández, T. Viveros-García, R. Fuentes-Ramírez, I.R. Galindo-Esquivel, Int. J. Hydrogen Energy 41 (2016) 9332–9343.

[22] a Vizcaino, a Carrero, J. Calles, Int. J. Hydrogen Energy 32 (2007) 1450–1461.

[23] I. Rossetti, C. Biffi, C.L. Bianchi, V. Nichele, M. Signoretto, F. Menegazzo, E. Finocchio, G. Ramis, A. Di Michele, Appl. Catal. B Environ. 117-118 (2012) 384–396.

[24] I. Rossetti, A. Gallo, V. Dal Santo, C.L. Bianchi, V. Nichele, M. Signoretto, E. Finocchio, G. Ramis, A. Di Michele, ChemCatChem 5 (2013) 294–306.

[25] B. ZHANG, W. CAI, Y. LI, Y. XU, W. SHEN, Int. J. Hydrogen Energy 33 (2008) 4377–4386.

[26] G. Centi, S. Perathoner, Catal. Today 148 (2009) 191–205.

[27] D. Chen, K. Christensen, E. Ochoa-Fernandez, Z. Yu, B. Totdal, N. Latorre, A. Monzòn, A. Holmen, J. Catal. 229 (2005) 82–96.

[28] K.O. Christensen, D. Chen, R. Lødeng, A. Holmen, Appl. Catal. A Gen. 314 (2006) 9–22.

[29] V. Gonzalez De La Cruz, J. Holgado, R. Pereniguez, A. Caballero, J. Catal. 257 (2008) 307–314.

[30] E. Finocchio, I. Rossetti, G. Ramis, Int. J. Hydrogen Energy 38 (2013) 3213–3225.

[31] V. Nichele, M. Signoretto, F. Menegazzo, I. Rossetti, G. Cruciani, Int. J. Hydrogen Energy 39 (2014) 4252–4258.

[32] V. Nichele, M. Signoretto, F. Pinna, E. Ghedini, M. Compagnoni, I. Rossetti, G. Cruciani, A. Di Michele, Catal. Letters 145 (2014) 549–558.

[33] V. Nichele, M. Signoretto, F. Pinna, F. Menegazzo, I. Rossetti, G. Cruciani, G. Cerrato, A. Di Michele, Appl. Catal. B Environ. 150-151 (2014) 12–20.

[34] I. Rossetti, J. Lasso, E. Finocchio, G. Ramis, V. Nichele, M. Signoretto, A. Di Michele, Appl. Catal. A Gen. 477 (2014) 42–53.

[35] I. Rossetti, J. Lasso, V. Nichele, M. Signoretto, E. Finocchio, G. Ramis, A. Di Michele, Appl. Catal. B Environ. 150-151 (2014) 257–267.

[36] T. Tago, H. Konno, S. Ikeda, S. Yamazaki, W. Ninomiya, Y. Nakasaka, T. Masuda, Catal. Today 164 (2011) 158–162.

[37] E.L. First, C.E. Gounaris, J. Wei, C. a. Floudas, Phys. Chem. Chem. Phys. 13 (2011) 17339.

[38] A. Chica, S. Sayas, Catal. Today 146 (2009) 37–43.

[39] J.F. Da Costa-Serra, M.T. Navarro, F. Rey, a. Chica, Int. J. Hydrogen Energy 37 (2012) 7101–7108.

[40] H. Inokawa, S. Nishimoto, Y. Kameshima, M. Miyake, Int. J. Hydrogen Energy 35 (2010) 11719–11724.

[41] H. Inokawa, S. Nishimoto, Y. Kameshima, M. Miyake, Int. J. Hydrogen Energy 36

(2011) 15195–15202.

[42] B.S. Kwak, J.S. Lee, J.S. Lee, B.H. Choi, M.J. Ji, M. Kang, Appl. Energy 88 (2011) 4366–4375.

[43] H. Inokawa, M. Maeda, S. Nishimoto, Y. Kameshima, M. Miyake, T. Ichikawa, Y. Kojima, H. Miyaoka, Int. J. Hydrogen Energy 38 (2013) 13579–13586.

[44] H.M. Rietveld, J. Appl. Crystallogr. 2 (1969) 65 – 71.

[45] R.W. Cheary, A. Coelho, J. Appl. Crystallogr. 25 (1992) 109 – 121.

[46] R.W. Cheary, A.A. Coelho, J.P. Cline, in:, J. Res. Natl. Inst. Stand. Technol., 2004, pp. 1–25.

[47] K.W.T. and D.G.C.B. Newsam J.M., Treacy M.M.J., Proc. R. Soc. A 420 (1988) 375 – 405.

[48] R.J. and V.S. Corma A., Navarro M.T., Rey F., Angew. Chemie Int. Ed. 40 (2001) 2277 – 2280.

[49] Will G., Powder Diffraction - The Rietveld Method and the Two Stage Method to Determine and Refine Crystal Structures from Powder Diffraction Data. Springer-Verlag Berlin Heidelberg., 2006.

[50] M. Trombetta, G. Busca, L. Storaro, M. Lenarda, M. Casagrande, A. Zambon, Phys. Chem. Chem. Phys. 2 (2000) 3529–3537.

[51] J.P. Marques, I. Gener, P. Ayrault, J.C. Bordado, J.M. Lopes, F.. Ramôa Ribeiro, M. Guisnet, Microporous Mesoporous Mater. 60 (2003) 251–262.

[52] A. Simon-Masseron, J.P. Marques, J.M. Lopes, F. Ramôa Ribeiro, I. Gener, M. Guisnet, Appl. Catal. A Gen. 316 (2007) 75–82.

[53] R. Baran, Y. Millot, T. Onfroy, J.-M. Krafft, S. Dzwigaj, Microporous Mesoporous Mater. 163 (2012) 122–130.

ACKNOWLEDGEMENTS

The valuable help of Dr. Alessio Sozzi and Dr. Giacomo Mariani is gratefully acknowledged.

The work was partly supported by H2FC European Infrastructure Project (Integrating European Infrastructure to support science and development of Hydrogen and Fuel Cell Technologies towards European Strategy for Sustainable Competitive and Secure Energy), project reference 284522.

TABLES

Table 1: Nomenclature, preparation parameters and main physical-chemical properties of the samples prepared. SSA = Specific Surface Area, reported as BET and micropore area from t-plot (the latter between parentheses).

Sample - Code	Initial Si/Al (atom/atom)	Post-treatment	Ni content (wt%)	Si/Al (mol/mol) EDX	SSA (m^2/g)
$Ni_{1.5}$HAlBEA(I) - 1	12.5	Calcination	1.5	13.6 ± 0.9	-
$Ni_{1.5}$HAlBEA(II) - 8	17	Calcination	1.5	14.5 ± 1.3	-
$Ni_{1.5}$HAlSiBEA(II) - 2	17	Partial deallumination	1.5	86 ± 16	-
$Ni_{1.5}$SiBEA(II) - 9	17	Deep deallumination	1.5	111 ± 14	320 (261)
$Ni_{0.6}$SiBEA(II) - 3	17	Deep deallumination	0.6	83 ± 15	-
$Ni_{3.0}$SiBEA(II) - 4	17	Deep deallumination	3.0	73 ± 40	322 (275)
$Ni_{0.7}$SiBEA(I) - 6	12.5	Deep deallumination	0.7	150 ± 46	361 (298)
$Ni_{1.0}$SiBEA(I) - 7	12.5	Deep deallumination	1.0	96 ± 15	-
$Ni_{4.0}$SiBEA(I) - 5	12.5	Deep deallumination	4.0	92 ± 21	329 (246)

Table 2: Rietveld elaboration of XRPD data. Quantitative distribution of the A, B and C polymorphs and relative accordance parameters R_p, R_{wp} and $R_{Bragg}{}^{*}$. The R_p and R_{wp} are profile fitting accordance parameters describing the goodness-of-fit of the profile. The R_{Bragg} describes the quality of the structure refinement and the obtained crystal parameters. For further details, see [49].

Sample	Phase	BEA A	BEA B	BEA C	R_{WP}	Rp
1	%	48.2(1)	32.4(1)	19.39(5)	3.9	3.01
	R_{Bragg}	1.77	1.62	1.99		
2	%	46.0(2)	34.8(1)	19.26(7)	4.18	3
	R_{Bragg}	1.15	0.82	1.23		
3	%	47.1(2)	33.0(1)	19.89(7)	4.62	3.61
	R_{Bragg}	1.68	1.09	1.74		
4	%	56.3(2)	24.60(9)	19.09(7)	4.41	3.32
	R_{Bragg}	1.85	1.86	1.99		
5	%	50.9(2)	29.2(1)	19.82(6)	4.24	3.27
	R_{Bragg}	1.58	1.13	1.67		
6	%	46.5(2)	35.3(1)	18.13(6)	4.24	3.27
	R_{Bragg}	1.74	1.04	1.8		
7	%	50.0(2)	30.8(1)	19.18(7)	4.53	3.51
	R_{Bragg}	1.84	1.38	1.94		
8	%	50.0(1)	33.01(9)	16.95(4)	4.44	3.55
	R_{Bragg}	1.72	1.35	1.92		
9	%	54.9(2)	25.0(1)	20.10(8)	4	3.07
	R_{Bragg}	1.62	1.59	1.72		

Table 3: Results of TPR-TPO-TPR cycles. The temperature range of each peak is reported in the first column for each analysis and the temperature of the maximum of the peak in the second one.

	TPR1			TPO			TPR2		
Sample	**Peak(s) (°C)**	**Maximum (°C)**	**Notes**	**Peak(s) (°C)**	**Maximum (°C)**	**Notes**	**Peak(s) (°C)**	**Maximum (°C)**	**Notes**
1	227-304	267		45-85	65		320-402	343	
				85-366	187	Main peak			
2	234-275	266		30-154	77		360-515	415	
	313-425	375	Main peak				515-636	601	
3	338-440	383		57-271	72		550-652	608	Very small
4	220-271	247		29-77	58		323-479	435	
	271-411	306	Main peak	77-355	258	Main peak	479-628	582	Main peak
5	225-350	294		28-97	54		169-277	195	
				97-379	277	Main peak	277-477	378	
							477-614	569	Main peak
6	209-342	279		28-97	35		456-637	579	
	342-676	438	Main peak	97-434	213	Broad			
7	340-407	360		117-407	286		328-605	557	
	407-549		Shoulder						
8	222-300	255		29-67	50		283-472	333	
	355-550	410	Main peak	67-300	101	Main peak			
9	325-430	343		28-67	50		465-641	607	Shoulder at 553°C
				67-300	113	Main peak			

Table 4: Results of activity testing at 750°C, GHSV = 1700 h^{-1}, H_2O/CH_3CH_2OH = 3 mol/mol, if not else specified. Effect of catalyst acidity.

750°C	9 (deep de-Al.)	2 (partial de-Al.)	8 (Calc. Si/Al =17)	1 (Calc. Si/Al=12.5)	1 *	Equilibrium value
CO/CO_2 Ratio	11.7 ± 1.1	-	46 ± 2	30.1 ± 1.2**	n.d. ***	2.44
C balance (%)	99 ± 3	98 ± 4	99 ± 4	99 ± 2	100 ± 1	-
Conv. H_2O (%)	47 ± 7	-	42 ± 12	46 ± 9	30 ± 2	52.7
Conv. EtOH (%)	100	100	100	100	100	100
H_2 productivity (mol/min kg_{cat})	0.73 ± 0.08	0.94 ± 0.02	0.72 ± 0.03	0.61 ± 0.09	0.61 ± 0.09	1.0
S_{CH3CHO} (%)	-	2.4 ± 0.3	-	-	-	-
S_{CH4} (%)	5.9 ± 0.3	1.9 ± 0.3	4.8 ± 0.8	4.8 ± 0.5	4.7 ± 0.4	0.01
S_{C2H4} (%)	-	-	-	-	10 ± 2	-
* contact time = 3655 h^{-1}						
** CO/CO_2 decreased to 6.6 ± 0.7 decreasing temperature to 625°C						
*** CO_2 not detected during the whole test						

Table 5: Results of activity testing at 750°C, GHSV = 1700 h^{-1}, H_2O/CH_3CH_2OH = 3 mol/mol, if not else specified. Effect of Ni content.

	Initial Si/Al = 17 (atom/atom) + deep deallumination			Initial Si/Al = 12.5 (atom/atom) + deep deallumination			
750°C	3	9	4	6	7	5	Equilibrium value
Ni (wt%)	0.6	1.5	3	0.7	1	4	
CO/CO_2 Ratio	38 ± 5*	11.7 ± 1.1	3.9 ± 0.3	39 ± 6	18 ± 1	2.4 ± 0.3	2.44
C balance (%)	99 ± 2	99 ± 3	99 ± 4	98 ± 2	96 ± 2	97 ± 4	-
Conv. H_2O (%)	35 ± 2	47 ± 7	52 ± 4	25 ± 3	41 ± 10	57 ± 7	52.7
Conv. EtOH (%)	100	100	100	100	100	100	100
H_2 productivity (mol/min kg_{cat})	0.73 ± 0.03	0.73 ± 0.08	0.82 ± 0.03	0.70 ± 0.04	0.79 ± 0.03	0.87 ± 0.08	1.0
S_{CH3CHO} (%)	-	-	-	-	-	-	-
S_{CH4} (%)	8 ± 3	5.9 ± 0.3	3.8 ± 0.6	6.5 ± 0.4	6.4 ± 0.3	3.5 ± 1.5	0.01
S_{C2H4} (%)	1.2 ± 1.1	-	-	2.5 ± 1.7	-	-	-
H_2/CO Ratio	1.9	1.85	2.53	1.9	2.04	3.25	3.23
* CO/CO_2 decreased to 18 ± 2 at 625°C but the selectivity to ethylene and aceteldehyde increased to 39% and 13%, respectively							

FIGURES

Fig. 1: XRD patterns of the prepared samples.

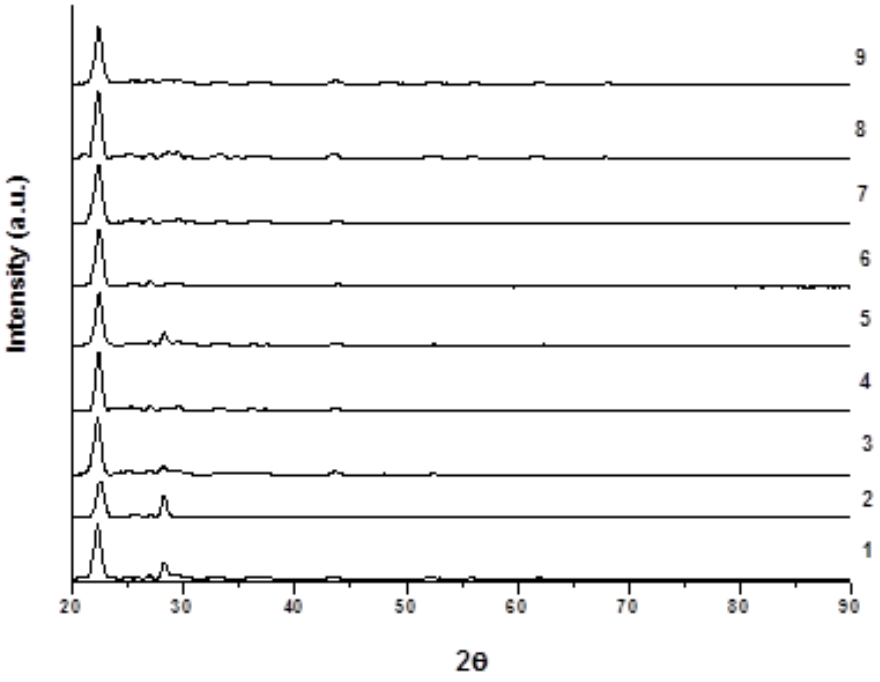

Fig. 2: TPR-TPO-TPR cycle of sample 9.

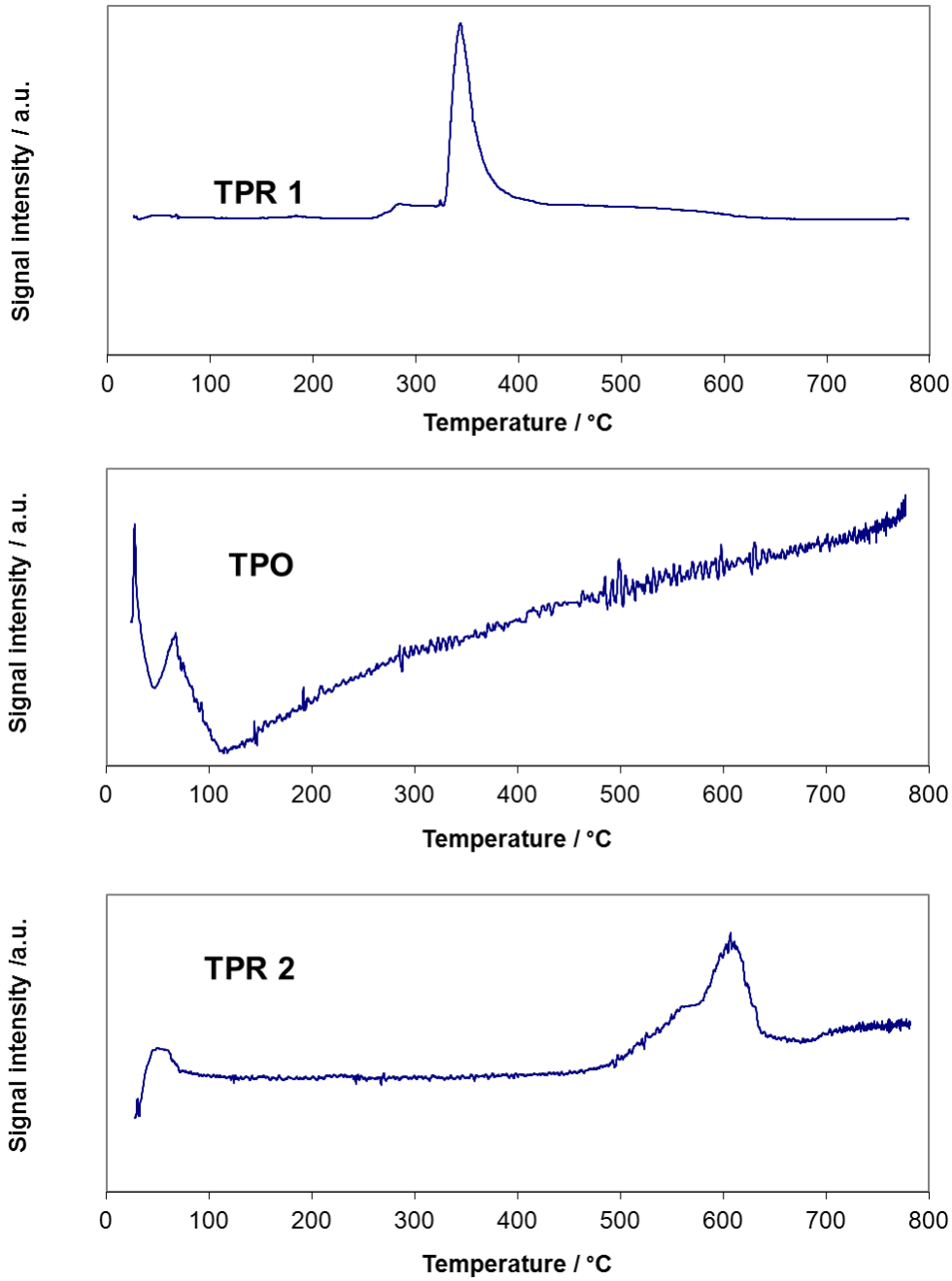

Fig. 3: TEM micrographs of samples a) with variable Ni loading, b) variable Si/Al ratio, c) sample 1 reduced at 800°C. Marker size 100 nm. Ni particles evidenced by arrows when needed.

a)

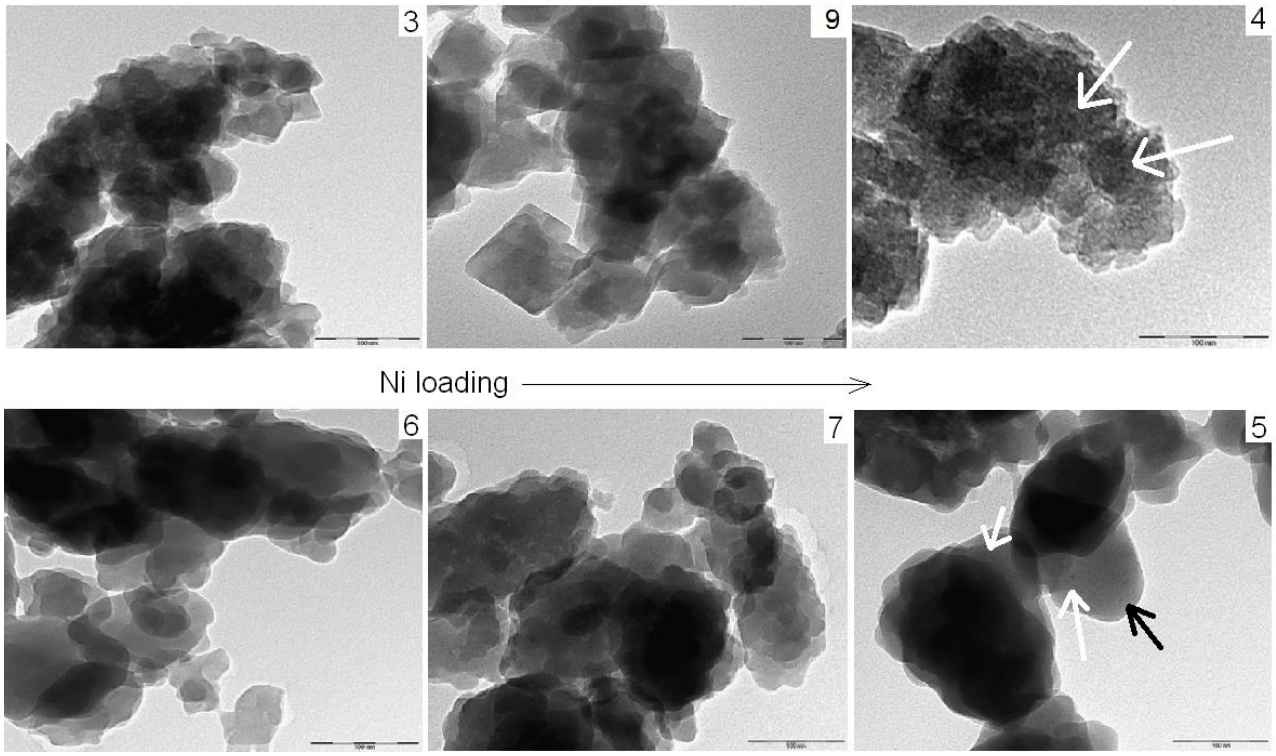

b)

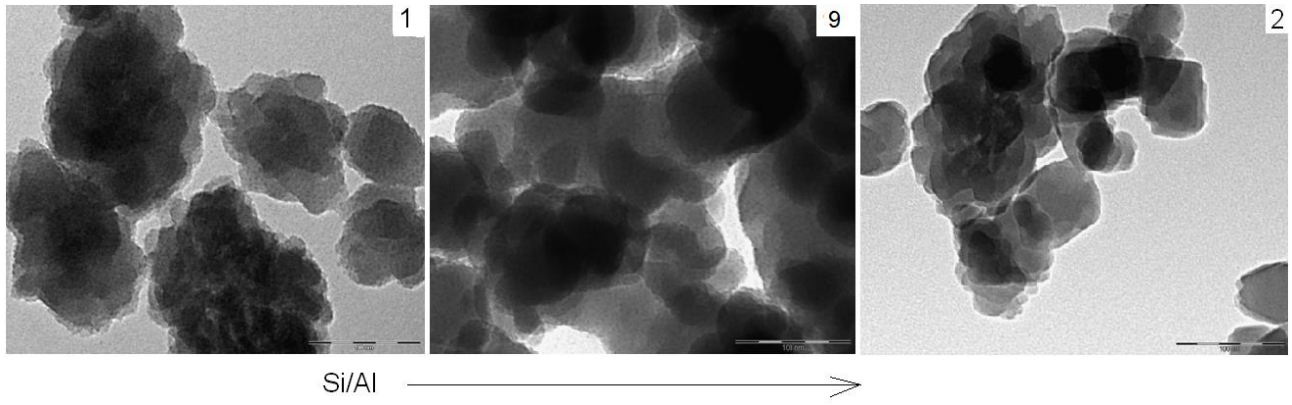

c)

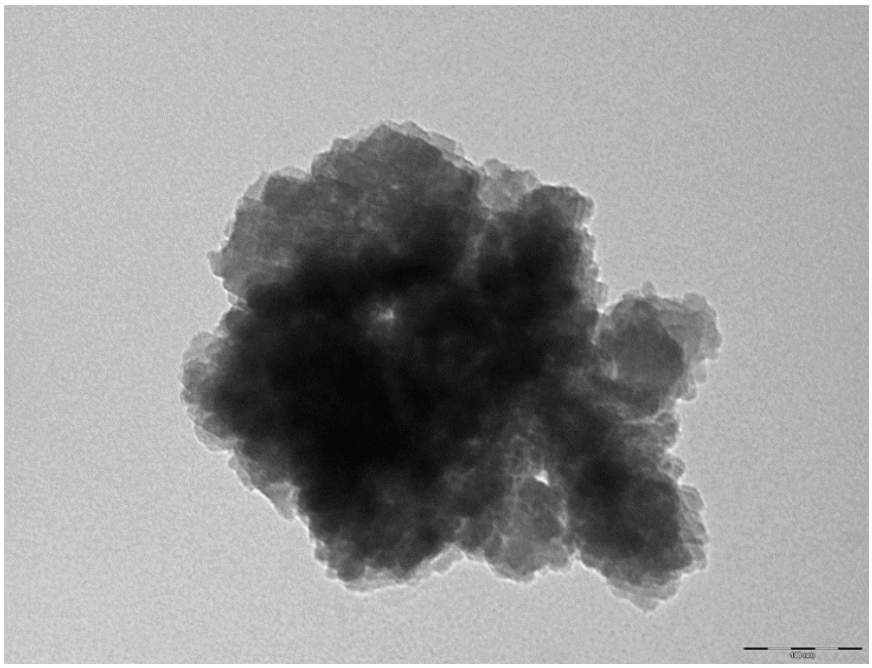

Fig.4: FT IR spectra of samples 1, 2, 3, 8 and 9 after outgassing at 500°C. OH stretching region.

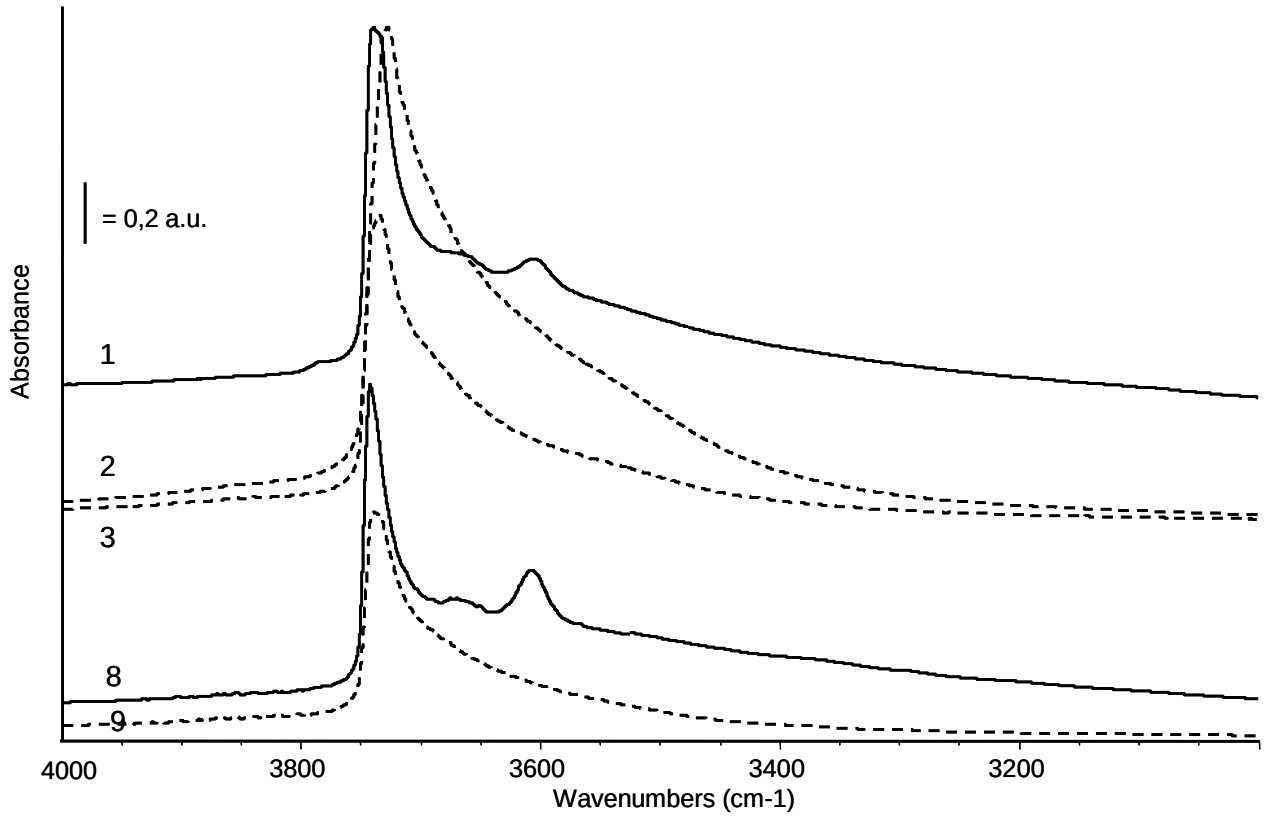

Fig. 5: Effect of Ni loading on selectivity to CH_4 (full symbols, left axis) and activity for the WGS reaction (empty dots, right axis).

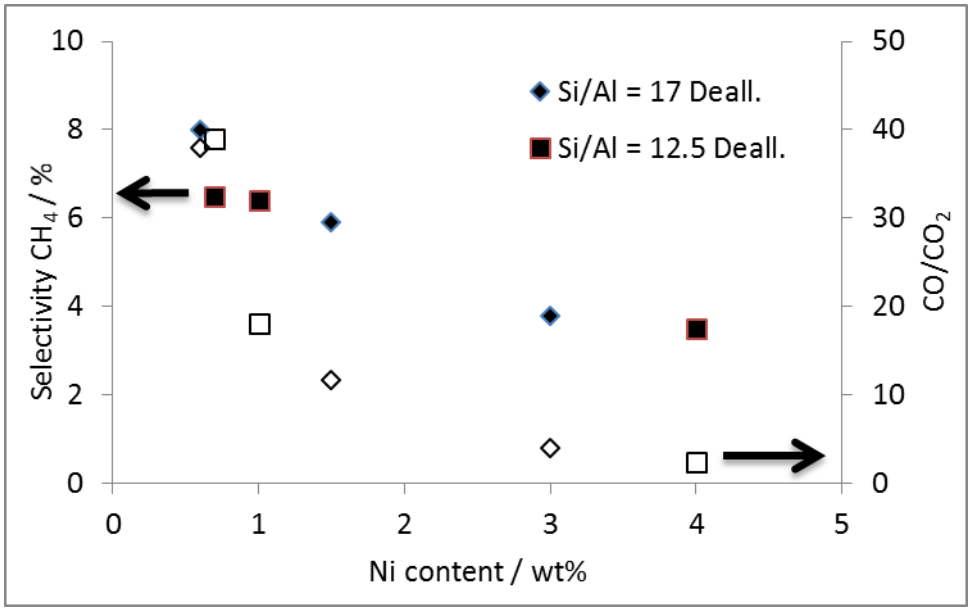

Fig. 6: Effect of Ni loading on the conversion of H_2O (full symbols, left axis) and H_2 productivity (empty dots, right axis).

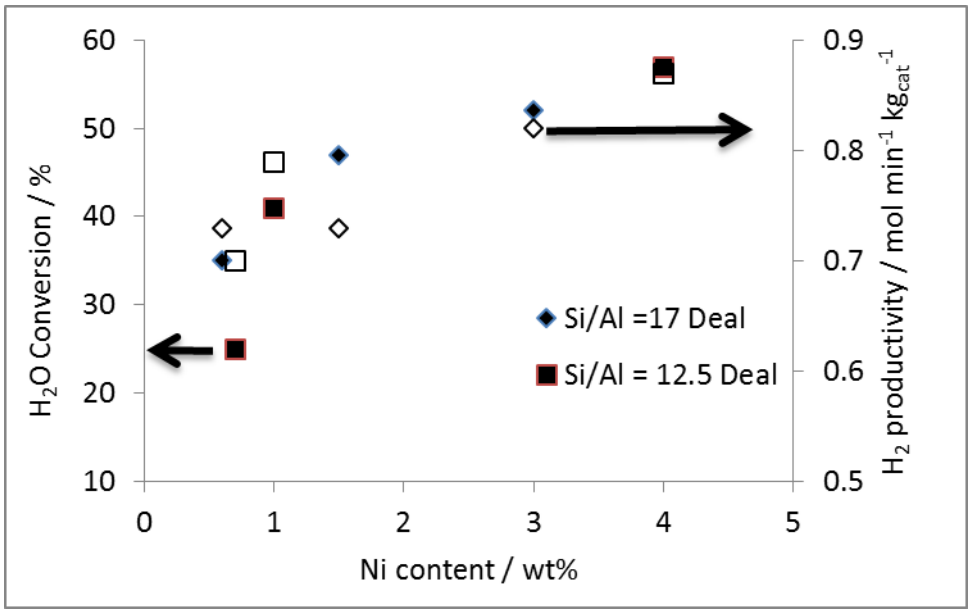

Fig. 7: Products distribution (molar fractions) vs. time-on-stream for selected samples at increasing Ni loading, same acidity, tested at 750°C, H_2O/CH_3CH_2OH = 3 mol/mol. a) sample 6; b) sample 5. CO fraction reported on right vertical axis, all other species on the left one. H_2 as balance.

a)

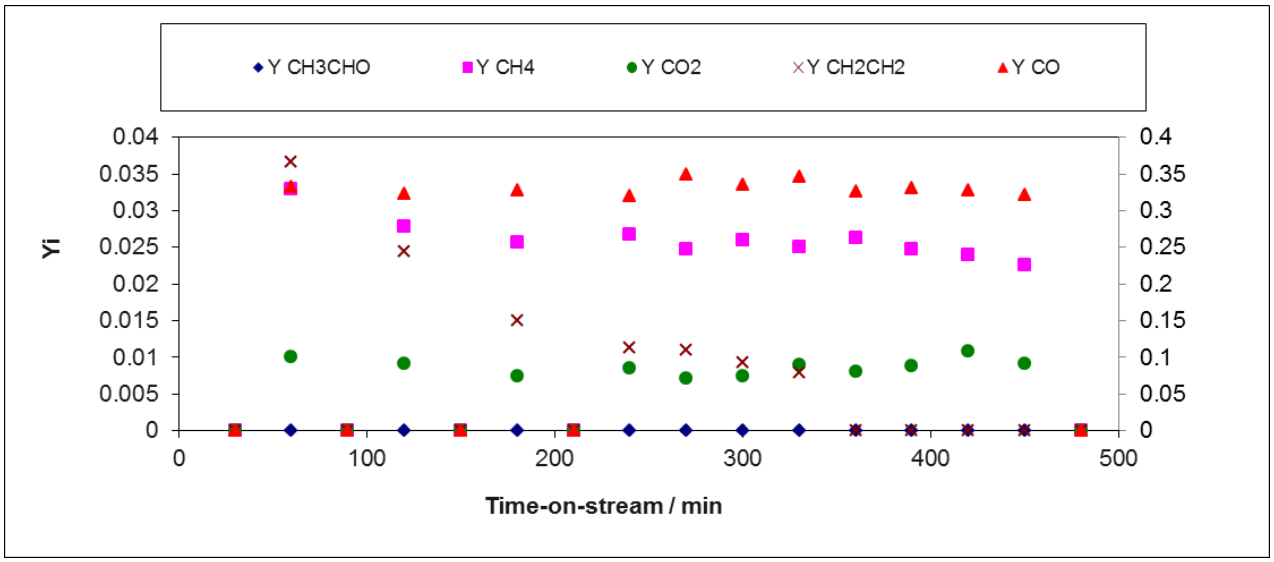

b)

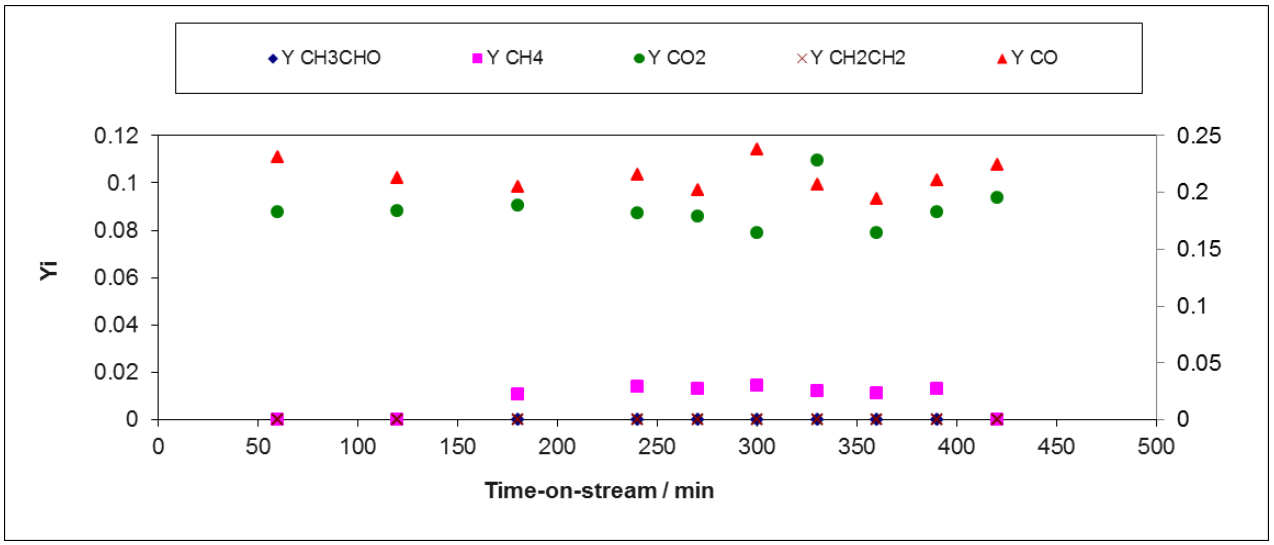

Fig. 8: Dependence of H_2/CO molar flows in the steam reformer effluent on Ni loading.